

**VALIDATION OF MARITIME SPECTRAL FEATURES**

By

Matthew J. Hubler

Submitted to the

Faculty of the College of Arts and Sciences

of American University

in Partial Fulfillment of

the Requirements for the Degree

of Master of Arts

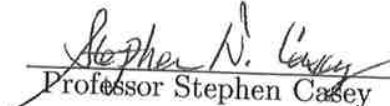
In

Mathematics

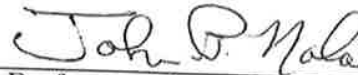
Chair:



Professor Michael Robinson



Professor Stephen Casey



Professor John Nolan



Dean of the College

April 29, 2014

Date

**VALIDATION OF MARITIME SPECTRAL FEATURES**

By

Matthew J. Hubler

Submitted to the

Faculty of the College of Arts and Sciences

of American University

in Partial Fulfillment of

the Requirements for the Degree

of Master of Arts

In

Mathematics

Chair:

\_\_\_\_\_  
Professor Michael Robinson

\_\_\_\_\_  
Professor Stephen Casey

\_\_\_\_\_  
Professor John Nolan

\_\_\_\_\_  
Dean of the College

\_\_\_\_\_  
Date

2014  
American University  
Washington, D.C. 20016

© COPYRIGHT

by

Matthew J. Hubler

2014

ALL RIGHTS RESERVED

# VALIDATION OF MARITIME SPECTRAL FEATURES

by

Matthew J. Hubler

## ABSTRACT

In 1991 a research team led by Klaus Hasselmann developed a general technique to build synthetic aperture radar (SAR) spectra from scans of the ocean surface; however these techniques were verified on older equipment. The algorithms input a SAR spectrum from an ocean spectrum, an inversion from SAR spectrum to ocean spectrum, and determine the threshold of the azimuthal cutoff. Originally designed for platforms that have since fulfilled their missions, the question remains as to whether the algorithms are valid with newer systems such as TerraSAR-X operated by German Aerospace Centre (DLR). One of the larger differences that may skew data analysis by these algorithms is that TerraSAR-X has much finer resolution, pixels being on the scale of 5-10 meters (or less), while older satellites returned images with pixel scaling on the order of kilometers. The finer pixel scaling allows for more detail to be recovered and analyzed, specifically the individual waves on the ocean surface become visible.

To that end, algorithms developed for older satellites will be employed on data collected from TerraSAR-X and compared to ground truth data in order to assess the compatibility of existing algorithms. During the course of the validation, several sets of code, written in Matlab, will be employed and discussed, each providing a different approach, more focused results. In aggregate a clearer picture will emerge describing

the accuracy that older algorithms have with newer machinery. The imagery data, being satellite borne, comes with individual collection geometry that needs to be addressed in the processing as well, currently through parsing the accompanying metadata. The determination that these algorithms indeed work with newer systems and the validation of an azimuthal cutoff demonstrate that little fine tuning of older algorithms is needed at these higher resolutions.

While the Hasselmann algorithms become cumbersome to use, a new approach to the algorithms yield useful quantifiable measurements. Thus combination of these new algorithms, buoy ground truth data, and more recent SAR technology deliver a powerful analytical tool. The eventual result of these algorithms could apply to meteorology, commercial shipping, disaster planning and recovery, ecology, and a vast assortment of other fields that would seek the wind patterns in open ocean scenes.

## ACKNOWLEDGEMENTS

I want to thank Dr. Michael Robinson, for overseeing the greater project this thesis stems from, my colleagues, since their work has enriched my own, the American University Vice Provost for Graduate Studies and Research, for funding Project Ocean Winds, the German Aerospace Center (DLR), for data provision, and my family and friends, for calming me during those minor meltdowns.

## TABLE OF CONTENTS

ABSTRACT . . . . .	ii
ACKNOWLEDGEMENTS . . . . .	iv
LIST OF TABLES . . . . .	vii
LIST OF FIGURES . . . . .	viii
CHAPTER	
1. INTRODUCTION . . . . .	1
2. BACKGROUND . . . . .	6
Satellite Imaging and SAR Advancement . . . . .	6
Azimuthal Displacement . . . . .	11
On a Nonlinear Mapping . . . . .	14
3. CONVERTING OCEAN SPECTRA TO SAR IMAGE SPECTRA . . . . .	16
Modulation Transfer Functions . . . . .	16
Frozen Surface . . . . .	17
Object Motion Contribution . . . . .	19
Relating an Image and Its 2D Fourier Transform . . . . .	20
4. CONVERTING FROM SAR IMAGE TO OCEAN SPECTRA . . . . .	23
An Iterative Approach . . . . .	23
A New Direction . . . . .	26
5. AZIMUTHAL CUTOFF FACTOR . . . . .	27

Theoretical Description of Azimuthal Cutoff . . . . .	27
Empirical Data Sources . . . . .	28
Validation . . . . .	31
6. CONCLUSIONS, CONTINUATION, AND FUTURE PLANS . . . . .	34
APPENDIX	
A. ABBREVIATIONS AND ACRONYMS . . . . .	35
REFERENCES . . . . .	36

## LIST OF TABLES

Table		Page
1.	Summary of Ground Truth Buoys . . . . .	30
2.	Summary of Azimuthal Cutoff Calculations . . . . .	33

## LIST OF FIGURES

Figure	Page
1. Artist Rendition of TerraSAR-X in Orbit . . . . .	7
2. Artist Rendition of Seasat During 1978 Orbit . . . . .	8
3. Artist Rendition of SIR-B in 1984 Orbit . . . . .	9
4. Overview Diagram of Azimuthal Displacement in SAR Imaging. . . . .	11
5. Azimuthal Displacement Example With Visible Smearing . . . . .	12
6. Orbital velocity of a Wave is the Velocity Vector Compment in the Direction of Motion. . . . .	13
7. Visual Representation of How Components in the Conversion Interact	17
8. Matching Coefficients of Spectra Constitutes the Desired Relationship	21
9. Generated SAR Spectrum with Base Geometry Inputs. . . . .	22
10. A Diagram of the Base Geometry Used in Testing . . . . .	22
11. Visual Representation of How Components in the Inversion Process Interact . . . . .	24
12. Ocean Spectra Processed from the same SAR Swath Using 30°, 37°, and 42° Incidence Angles (respectively) . . . . .	25
13. Scenes of Data Collections and Associated Images . . . . .	29
14. Spectra of an Original SAR with Visible Spectral Width (left) and Preview Image with Visible Spectral Peaks (right). . . . .	32
15. Buoy Spectra Used in Measurement for Azimuthal Cutoff Computation.	33

# CHAPTER 1

## INTRODUCTION

In 1957 the first artificial satellite began to orbit Earth. Sputnik 1 spent three months on mankind's maiden voyage to the cosmos, but the Space Race rapidly fueled scientific advances. Nowadays, we use satellites constantly throughout the day. Whether talking on your cell phone or having GPS map out your journey, satellites have been a luxury to most of the younger generations. However, there is always improvement to be made and new techniques to be tested. Mankind has come a long way since the Soviet Era's first satellite, but we still strive to modernize and employ our technologies to better our lives.

The context for this particular research comes from a larger project at American University. Under the leadership of Dr. Michael Robinson, three graduate students and one undergraduate are attempting to develop algorithms for using high resolution synthetic aperture radar (SAR) satellite imagery to measure waves and discern the wind speed and direction from these waves [Robinson (2013)]. With applications ranging from military to meteorological and commercial to leisure, the demand for accurate open sea wind models drives the research.

The main contributions of this thesis are threefold. To begin the process, I implemented and tested a conversion from ocean spectrum to SAR image spectrum. Next, I programmed the inversion process, taking SAR image spectra to ocean spec-

tra. Both revealed limitations in processing and areas for future improvement. Finally, I took the Hasselmann expression for the azimuthal cutoff factor arising from surface wave motion and validated it against buoy ground truth. The validation of the azimuthal cutoff was the first known instance of such verification using a high resolution space-based radar.

There are, of course, limitations to the project. Since open sea scenes are the primary focus, ground truth validation becomes exceedingly difficult. Because man made structures and objects, such as oil platforms and boats, create interference in spectrum processing, we rely on smaller meteorological buoys for ground truth data. We are also limited by the capabilities of the satellite we are using, TerraSAR-X. Currently there is at most dual polarization and right looking imaging available for scientific research. Thus the polar orbit of TerraSAR-X limits our time windows, since typically the closest passes of an area occur three days apart, and scenes too close to the poles are unavailable.

Our process takes a satellite image, metadata, and ground truth and computes a variety of parameters that yield angular and clustering values, inherent in the wind direction and speed, respectively. However, we eventually we need to extract several parameters from the scene to begin with and keep in mind the limitations of our platform. Thus the early focus was to identify problem areas and begin to test the impact and limitations these problems bring about.

Further limitations come from being a small group at a university. We have limited computational power, limited manpower, and high turnover as students graduate. Thus the entire project must have easily connectible pieces contributed by each member.

For many years, these limitations and constraints seemed too much for many small institutions to use satellite borne imagery to do research. However, the process

has become more feasible for more researchers. Thus, the discussion that satellite imaging should be ‘exclusively’ done by large, well-funded institutions, governmental and commercial alike, no longer applies. Hence, on top of describing and walking through the research in this paper, it should be noted that the work being done at American University proves that smaller teams of researchers may have powerful impacts on these less developed fields.

Prudently, the discussion will start with satellite imaging and advances in synthetic aperture radar platforms. A general knowledge of the strip map imaging mode and how multi look ground range detected (MGD) representation of data benefit the work being done. Discussing the modes in use raises the topic of TerraSAR-X being an evolutionary step in SAR technology. Resolution and polarity will take center stage in this conversation as that is the true benefit over previous platforms.

The seminal paper that drove this particular research, ‘On the Nonlinear Mapping of an Ocean Wave Spectrum Into a Synthetic Aperture Radar Image Spectrum and Its Inversion’ [Hasselmann and Hasselmann (1991)], collected data by SAR from the Seasat satellite and the shuttle borne SIR-B mission were used to develop a series of algorithms. Hasselmann’s algorithms stay true to the paper’s name. First a conversion from ocean wave spectrum to SAR image spectrum is presented. Then Hasselmann derives an expression for the azimuthal cutoff factor of any given image. The paper proceeds to exhibit and expand upon an iterative process that brings a SAR image spectrum back to the ocean wave spectrum. While the manipulations work well on Seasat and SIR-B data, since their models were validated using these data sets, the question remains as to the accuracy and precision of the algorithms when used on higher resolution data.

Each process demands considerable attention. We start with the how to convert an ocean wave spectrum into a SAR image spectrum. While broken up into

frozen surface contribution and motion effects, the heart of the forward conversion ('forward' here is a reference to being given ocean wave spectrum as input) lies in modulation transfer functions (MTFs). Specifically the process requires combining two MTFs into a single MTF, tilt and hydrodynamics into real aperture radar (RAR). In addition to these MTFs, the conversion between ocean spectra and SAR image spectra include the platform velocity and the intensity of reflectivity at each pixel.

The inversion of the above process, an iterative procedure, requires much regularization, as azimuthal cutoff and  $180^\circ$  ambiguity leads to data loss. Minimizing differences between projected and actual spectra requires cumbersome computations. Hasselmann's quasi-linear solution, therefore, has proven inefficient. A new approach has been proposed by this team after examining the iterative process, which will hopefully lead to faster processing. Such an inversion would go pixel by pixel instead of processing entire images several times over.

The central contribution of this thesis is the confirmation of the azimuthal cutoff factor expression. With the Doppler effect taking objects out of scene, this measurement must be accounted for. Although displacement cutoff may be measured directly from an ocean spectrum, run time considerations suggest that a parametric computation is more efficient.

Much goes into the computation of the cutoff, as several branches of physics contribute theoretical aspects to the formula. The benefit of this research comes from ground truth verification using measurements that are readily available. Buoys were chosen as scene centers with the express intention to use the data to hone our algorithms and collect data to compare the performance of the Hasselmann algorithms. Thus scenes were first chosen in the Pacific Northwest near Tillamook, OR, USA and the Gulf of Mexico, with additional scenes chosen in the Gulf of Maine, Alaska,

Puerto Rico, and Martinique. The buoys allowed the validation of the cutoff, which in turn allows the identification of visible spectral features in a given collection.

## CHAPTER 2

### BACKGROUND

In order to fully understand the conversion processes, this chapter will address several background topics. Prudently, the advancement in SAR imaging technology starts off with some comparison to former platforms. Discussion of the phenomenon of azimuthal comes next due to extensive involvement in all phases of processing. Finally, a presentation of the 1991 paper by Hasselmann motivates the experiment and its design.

#### *Satellite Imaging and SAR Advancement*

At the core of this thesis is the concept of radar. Radar, short for radio detection and ranging, consists of unit emit radio waves that hit and scatter. Since a small amount of the waves return to the antenna, a receiver set up allows for the object to be tracked and the distance of the object to be measured. Since its development before World War II, radar has greatly evolved. Beside the military purposes, radar usage has expanded to the scientific community and has been made mobile by mounting radar systems on a variety of platforms. Real aperture radar (RAR) transmits a beam perpendicular to the platform's motion and builds an image based upon sequential strips of scanned terrain. Unfortunately, RAR does not take into account relative motion in an image. Synthetic aperture radar (SAR) corrects for this motion. Since SAR takes motion of objects in a scene (called 'scatterers') into account,



Figure 1. Artist Rendition of TerraSAR-X in Orbit

a finer resolution and more accurate image may be generated.

Compared to its predecessors, TerraSAR-X [Refer to Figure 1], operated in conjunction with TanDEM-X by the German Aerospace Center (DLR), embodies technological advancements seen in the last few decades. TerraSAR-X, launched in 2007, provides excellent instruments and flexibility for scientific advancement. In addition, the comparison between TerraSAR-X and other modern general purpose satellites, such as Radarsat-2, supports the decision to work with TerraSAR-X data. (Radars will be discussed chronologically here, Seasat to Radarsat-2)

NASA's first SAR satellite committed to oceanography was launched in 1978 and lasted for a little over 100 days in orbit [NASA (a)]. Unfortunately, a circuitry issue decommissioned Seasat [Refer to Figure 2] a few months after beginning its mission. However, the data collected made some impact scientifically, including in the Hasselmann paper to develop and verify their algorithms. Seasat had two goals for its mission, the first was to monitor global ocean wave activity and the second was to observe changes in the polar regions, both temperature and ice conditions. Thus Seasat's look angle, remained fixed, which limited the range of incidence angles, the angle at which the radar beam contacts a target. Additionally, the platform only



Figure 2. Artist Rendition of Seasat During 1978 Orbit

emitted and received beams in the horizontal polarization. The maximum resolution for images on Seasat products was 25m by 25m per pixel in 100km swaths. Many later satellites incorporate instruments that were based upon Seasat's devices.

After the successful imaging of Seasat, NASA sought to continue its research mission and optimize efficiency. Besides furthering our scientific understanding of satellite imaging, the shuttle borne mission Shuttle Imaging Radar (SIR) A and SIR-B tested the validity of space shuttles as radar platforms [NASA (b), NASA (c)]. Launched three years apart in the early 1980s, both missions featured HH polarized equipment. The instruments on SIR-B were slightly more sophisticated and their specifications are slightly more relevant to the conversation than those on SIR-A. Many researchers clamored for the data taken during SIR-B, from its radar operations. The key lies in that SIR-A operated its SAR unit for eight hours while the more advanced SIR-B looked at multiple scenes multiple times while orbiting nearly fifty cycles. The finest resolution of these 20-40km swaths came in at 20m by 16m. These shuttle missions were a great advance in SAR platform understanding, however the exclusivity of the research team indicated that SAR imaging would be an unapproachable subject for smaller or less well funded institutions. Additionally, the program could only run while a shuttle was in orbit with the platform extended, meaning limited data take windows and many groups looking to have their images



Figure 3. Artist Rendition of SIR-B in 1984 Orbit

taken and data collected. Thus it appeared that unmanned satellites were preferable in order to widen the access to data and further science as a whole.

A few months after the launch of TerraSAR-X, the Canadian Space Agency (CSA) deployed Radarsat-2 [CSA (CSA)]. While several countries have launched all purpose satellites, Radarsat-2 and TerraSAR-X lead in notability. Radarsat-2 is the second stage of Canadian general purpose platforms. While the Radarsat Constellation Mission, planned for 2018, has three satellites providing data, each will be able to supply the same kind of imagery as Radarsat-2 currently collects.

TerraSAR-X and Radarsat-2 have similar capabilities. With a slightly finer highest resolution and more available imaging modes in scientific observations, Radarsat-2 sacrifices scene swath size for resolution. The trade off means that scientist must choose between seeing a large field (170km) with resolution in tens of meters for analysis or seeing the extremely fine detail with resolution of meters in a considerably smaller (18-20km) scene. Both satellites have the capability of dual and quad polarization, however quad polarization requires time to convert the antennae to and is therefore not as readily available.

Looking at the specifications associated with the aforementioned satellites, TerraSAR-X [Werninghaus (2009), Zink (2010)] plainly becomes a candidate to represent the newest class of general purpose SAR platforms. The flexibility in imaging modes, high resolution over large swaths and polarization capabilities represent the characteristics of a SAR satellite needed for this and many other scientific ventures. Moreover, since the capabilities of other general purpose SAR platforms closely rival TerraSAR-X, we have the ability to extrapolate our results and apply them to other SAR imaging sources. Hence the results of this thesis and other work done with TerraSAR-X lend themselves more generally to SAR platforms with similar specifications.

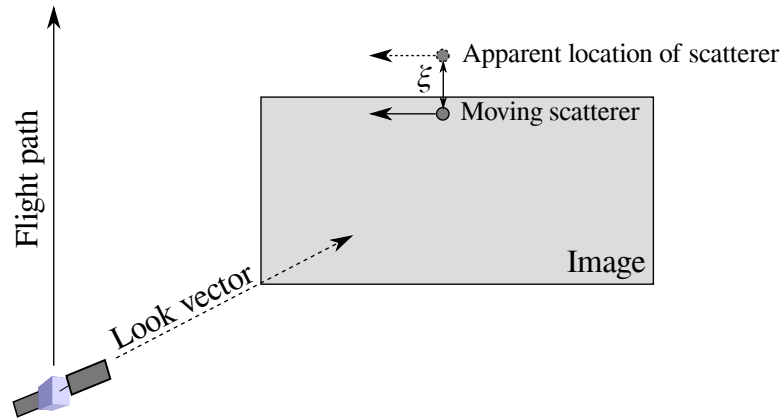


Figure 4. Overview Diagram of Azimuthal Displacement in SAR Imaging.

### *Azimuthal Displacement*

In anticipation of discussing Hasselmann's paper, the phenomenon of azimuthal displacement must be described. Azimuthal displacement occurs when objects in a SAR scene are moving. The easiest way to understand azimuthal displacement is to think of the Doppler effect. When two objects are in relative motion, a car and a police cruiser for example, the sound emitted from one to the other changes based upon relative position. For example, the siren from a police car as it passes has a noticeably different tone. Azimuthal displacement is Doppler frequency effect. The azimuth direction runs parallel to the flight path. Much as the police siren sounds differently, the location of the wave in the SAR image appears differently than in actuality.

Satellite images mark the positions of objects based upon their azimuth or doppler coordinate and a range coordinate. Imagine that a satellite is moving with a flight path due north while looking to the right and a wave traverses the ocean in a westerly direction. The wave would appear to be more northward than actual. If the wave was traveling easterly instead, it would shift southward in the SAR image. All

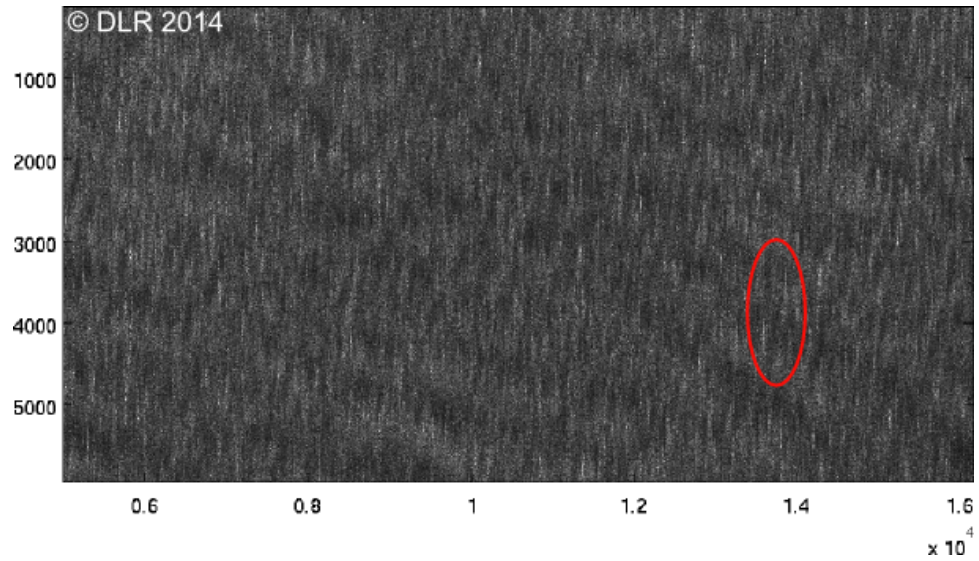


Figure 5. Azimuthal Displacement Example With Visible Smearing

shifts reverse when the satellite is looking left and still traveling due north. (Refer to Figure 4.)

These nonlinear distortions of our images have the potential to derail processing. In several images, we encountered boats and man made structures that, besides lighting up and presenting themselves as extremely obvious, may have displaced waves in the intensity data. Thus recovery of information from these pixels is extremely difficult and skews the processing enough to be noticeable. The other inherent danger resides out of our scene. The displacement may be great enough to take waves out of blocks of processed data or bring waves from outside the scene into our viewing window.

Luckily, a rather simple formula represents the azimuthal displacement,

$$\xi = \frac{\rho}{U}v. \quad (2.1)$$

Thus azimuthal displacement  $\xi$  can be computed by multiplying the orbital velocity

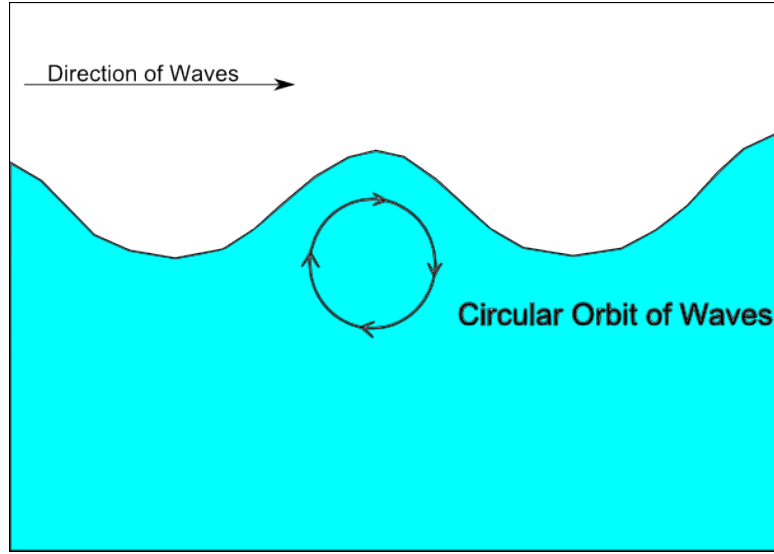


Figure 6. Orbital velocity of a Wave is the Velocity Vector Component in the Direction of Motion.

of the waves  $v$  by the ratio of slant range  $\rho$  and the platform velocity  $U$ . Slant range simply means the distance between the antenna and the scene; platform velocity is just the speed of the SAR unit itself. However, the orbital velocity of the waves is the component of wave velocity in the orbital direction (Refer to Figure 6.), which has its own associated formula:

$$v = \sum_k T_k^v \zeta_k e^{ikr} + c.c. \quad (2.2)$$

where  $c.c.$  stands for the complex conjugate. In these formulas,  $r$  stands in for the ground to satellite vector and  $k$  represents the wavenumber at which we are currently computing. For the purposes of this thesis, wavenumber shall be described as the spatial frequency of the wave. Thus orbital velocity takes into account, the surface elevation of the wave,  $\zeta$ , at each wavenumber and a range velocity transfer function given by

$$T_k^v = -\omega \left( \frac{k_l}{|k|} \sin(\theta) + i \cos(\theta) \right). \quad (2.3)$$

A fair bit of geometry factors into the above transfer function. Besides relying on the wavenumber, the function accounts for the wavenumber component in the look direction of the satellite  $k_l$  as well as the incidence angle for that particular image  $\theta$ . The operating frequency of the satellite  $\omega$  also contributes to the function.

Stepping back from the mathematics and technical details, azimuthal displacement's dependence on geometry needs to be clarified. With the exception of surface elevation and operating frequency, all other elements follow from the geometric organization of the scene, waves, and satellite in conjunction. Relative motion and collection parameters drive how objects such as ocean waves appear shifted in the SAR image. Thus every SAR image has its own azimuthal displacement computation, meaning the process must be highly generalized as to work with metadata and must be made relatively simple to compute.

### *On a Nonlinear Mapping*

After the launch of Seasat and the success of SIR-B, a new wealth of data by satellite borne SAR became available to researchers. While several groups focused on specific pieces of processing, the Hasselmanns wished to tackle a more general problem. Similar to the research being conducted by Project Ocean Winds at American University, the Hasselmann paper compares findings with buoy spectra data.

Klaus Hasselmann has headed up some major research centers in his career. Best known for his work on climate variability, Hasselmann held the Director position at the Institute of Geophysics, Max-Planck-Institute of Meteorology, and the German Climate Computer Centre. His work in oceanology landed him a brief stint at Woods Hole Oceanographic Institution and Cambridge University. Much of his work centers

around ocean waves as climate predictor and how to analyze wave models in various context.

The 1991 paper specifically sought to address the mathematics behind ocean spectra and SAR image spectra. Since many researchers had examined specific quantities related to the input functions, Hasselmann aggregated previous research in the process of algorithm development. In particular, Folkhart Feindt [Feindt (1985)] proved that there existed an appropriate feedback term in the hydrodynamic modulation transfer function, which was previously not included. Additionally, both Feindt and the Hasselmann reference work by W.C. Keller and J.W. Wright [Keller and Wright (1975)], who characterize a dampening factor in the same equation. Due to the small community producing high level work in the field, it should be noted that Keller and Wright were cited by both Feindt and Hasselmann, who also cited each other in their respective papers. Many other researchers were mentioned in through the entirety of the paper, however most focus on the modulation transfer functions that factor into the image processing.

## CHAPTER 3

### CONVERTING OCEAN SPECTRA TO SAR IMAGE SPECTRA

In order to understand how the ocean spectra and SAR image spectra relate, we implemented Hasselmann's conversion using the function call heirarchy shown in Figure 7. First, the image must be considered as two separate pieces, (1) a frozen surface with no motion and (2) a moving surface. Only by considering both scenarios do the actual mathematical representations make sense. Next the discussion progresses to Fourier series and its associated coefficients. These coefficients are the information that must be related between the two spectra. Finally, we will look at the actual relationship between the ocean spectrum and the SAR image spectrum and briefly talk about computation at the hear of the conversion.

#### *Modulation Transfer Functions*

The relationship between these two spectra come about from modulation transfer functions (MTFs). From physics, MTFs are a subfield of optical transfer functions (OTFs) and were developed to better call out contrasts in spectra. Simply stated, OTFs are Fourier transforms of point spread functions, or impulse responses of the optic in question (in our case the SAR). We derive a MTF by taking the absolute value of an OTF. While providing a more accurate description of the relationship bewtween spectra, these functions are inherently nonlinear. Hence the computation is more complex.

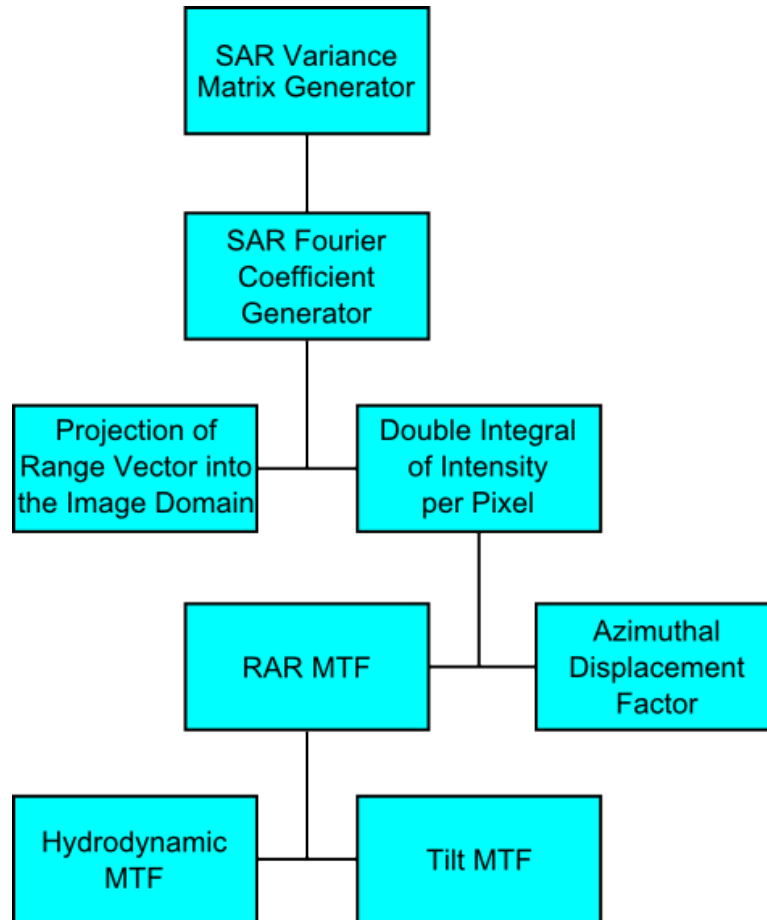


Figure 7. Visual Representation of How Components in the Conversion Interact

### Frozen Surface

The contribution to the conversion from a static (or 'frozen') surface comes in two parts. Both the elevation and the real aperture radar (RAR) MTF impact the values of a frozen surface.

The thought that elevation plays a role in ocean imaging may seem odd since we are looking at objects at sea level. However, 'elevation' calls out the heights of individual waves in scene. Consider two wave scenarios, a rather calm day with low waves and a turbulent stormy day with massive waves. In the first scenario, the term accounts for the fact that the waves all sit essentially at sea level. In the second, the

waves rise well above sea level and must be accounted for being so large. For each individual wavenumber, or in our case pixel, in the ocean spectrum, we denote the elevation as  $\zeta_k$ .

The majority of this section will be tracing the evolution of the RAR MTF that makes up the larger contribution. The RAR MTF itself has two components,

$$T_k^R = T_k^t + T_k^h. \quad (3.1)$$

Here  $T_k^t$  represents the tilt MTF, which changes based on polarization, and  $T_k^h$  stands for the hydrodynamic MTF. Recall that the subscript  $k$  represents the wavenumber at which the evaluation occurs.

The tilt MTFs rely on the incidence angle,  $\theta$ , and the wavenumber component in the look direction  $k_l$ . The VV polarization tilt MTF requires incidence angles less than 60 degrees,

$$T_k^t = 4ik_l \cot \theta (1 + \sin^2 \theta)^{-1} \quad (3.2)$$

The HH tilt MTF holds less restriction,

$$T_k^t = 8ik_l (\sin 2\theta)^{-1} \quad (3.3)$$

The work done by many other researchers lies in the hydrodynamic MTF,

$$T_k^h = \frac{\omega - i\mu}{\omega^2 + \mu^2} (4.5) k\omega \left( \frac{k_y^2}{k^2} + Y_r + iY_i \right). \quad (3.4)$$

Here appears the feedback term  $\mu$  and the constant defined by Keller and Wright (1975) and Feindt's feedback term  $Y_r + iY_i$  from his 1985 doctoral thesis. Recall that  $\omega$  stands for the operating frequency of the radar and that the axes are oriented so that  $x$  and azimuth (flight path) correlate. Hence  $k_y$  may be negative depending upon the look direction for the satellite.

Tracing the feedback term through Feindt's doctoral thesis [Feindt (1985)], we determine that  $Y_r + iY_i$  has been renamed from  $\nu\omega e^{i\phi\omega}$ . As Feindt mentioned, the phase factor  $\phi\omega$  is an experimental value. The variable  $\nu$  has the formula

$$\nu = \alpha \cdot \frac{\omega}{g} u^*, \quad (3.5)$$

where  $\alpha$  is a dimensionless constant (with a value of 0.1). Besides the gravitational constant  $g$ ,  $\nu$  relies upon the frictional velocity of the wind over the water  $u^*$ . Lange and Hühnerfuss [Lange and Hühnerfuss (1978)] allows us to calculate  $u^*$  via

$$\frac{u}{u^*} = \frac{1}{\kappa} \ln \left( \frac{z}{z_0} \right). \quad (3.6)$$

Recognizing  $\kappa$  as the Kármán constant with value of 0.41,  $z$  is the height of the anemometer, in this case on an oceanographic buoy. The wind speed measurement  $u$  also comes from buoy data. Lange and Hühnerfuss also present an equation for  $z_0$  depending on  $u^*$  and the viscosity of the air above the water  $\eta$ ;

$$z_0 = \frac{\eta}{u^*}. \quad (3.7)$$

Thus through experimental extrapolation, the feedback term derived by Feindt may be discerned. Hence combining these two MTFs, hydrodynamic and tilt, we arrive at the RAR MTF.

### Object Motion Contribution

To understand the motion effects of objects in scene, the use of a RAR MTF is inappropriate. After briefly recalling the previous discussion of azimuthal displacement, an additional factor will be added to the RAR MTF leading to the presence of a more suitable SAR MTF.

Azimuthal displacement occurs due to the relative motion of objects in scene and the satellite platform. The layering of azimuthal displacement peels back to reveal that at the lowest level the range velocity transfer function drives the phenomenon [Equation 2.3]. The geometry and parameters that further feed the displacement combine in the other factors as well.

In order to produce the SAR MTF, the bunching of ocean winds turns the RAR MTF into the SAR MTF.

$$T_k^S = T_k^R + T_k^{vb} \quad (3.8)$$

Where the velocity bunching transfer function,  $T_k^{vb}$ , is given by

$$T_k^{vb} = -i \frac{\rho}{U} k_x T_k^v \quad (3.9)$$

Notice that both components of the motion effects find themselves built by the range velocity transfer function. These motion factors have a profound impact for being so basic relative to the other contributors. With essentially just the range velocity transfer function the image produced goes from not registering motion to representing the complex movements of the ocean surface.

### ***Relating an Image and Its 2D Fourier Transform***

The relation between the spectra relies on some harmonic analysis. Fourier transforms convert functions from the space or time domain to the frequency domain. Periodic functions may be further decomposed into a sum, weighted by coefficients, of oscillating components, trigonometric functions or complex exponentials. These coefficients are what we relate between the ocean and SAR image spectra as in Figure 8.

Hasselmann goes through a long derivation of the proposed relation based upon

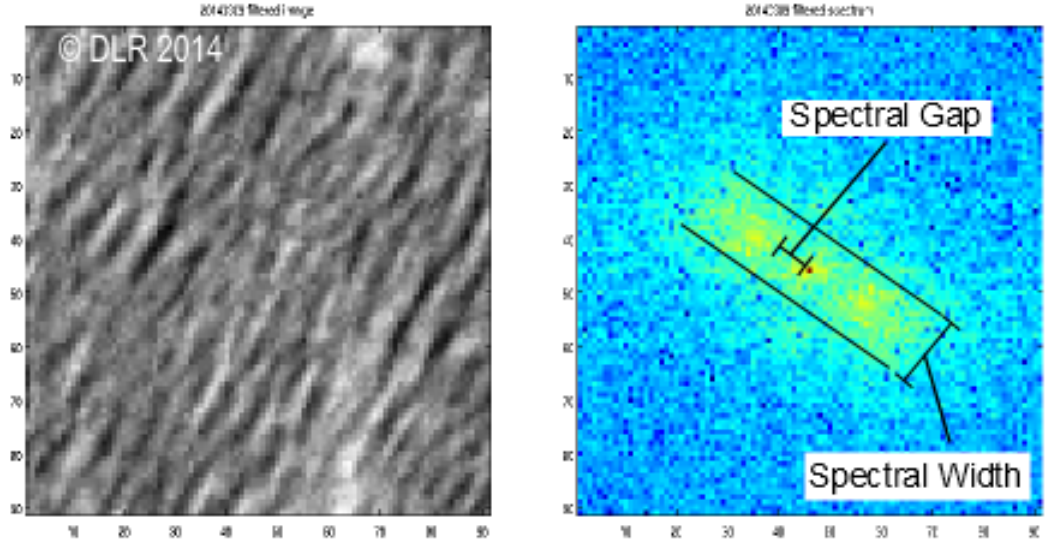


Figure 8. Matching Coefficients of Spectra Constitutes the Desired Relationship

the Seasat and SIR-B data. Eventually the following results as our relationship,

$$P_k^S = A^{-2} \iint_{\mathbb{I}} dr' dr'' (e^{-k(r'-r'')} - ik(\xi(r') - \xi(r''))) \cdot (1 + \sum_{k'} (T_{k'}^R \zeta_{k'} + T_{-k'}^{R*} \zeta_{-k'}^*) e^{ik'r'}) \cdot (1 + \sum_{k''} (T_{k''}^{R*} \zeta_{k''}^* + T_{k''}^R \zeta_{k''}) e^{ik''r''})$$

where A is the area of the image and  $\mathbb{I}$  is the entire image.

By coding this double integral into MATLAB using a rectangular estimation method, faster computation becomes available. Several of the images from Project Ocean Winds have been used to test the validity of the formula and produce appropriate SAR images (such as the one in Figure 9 using the geometry shown in Figure 10). However, small images are required with currently available computing power, since a 100 pixel by 100 pixel image requires several days to run. Fortunately, 25 pixel by 25 pixel and 50 pixel by 50 pixel take only a few minutes and a few hours, respectively.

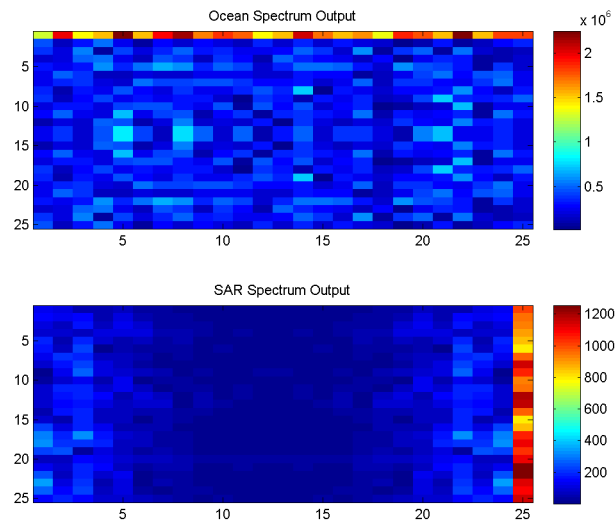


Figure 9. Generated SAR Spectrum with Base Geometry Inputs.

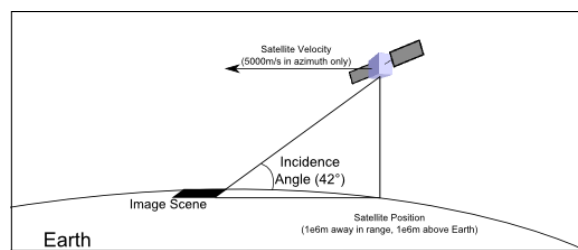


Figure 10. A Diagram of the Base Geometry Used in Testing

## CHAPTER 4

### CONVERTING FROM SAR IMAGE TO OCEAN SPECTRA

Now that the connection between the ocean and SAR image spectra has been discussed, an inversion scheme allows ocean surface conditions to be discerned from SAR images. Therefore we implemented Hasslemann's inversion according to the diagram in Figure 11. However, this process presents efficiency problems from the stand point of time and computing power. Therefore, a pixel by pixel method, under development, looks to solve those inefficiencies.

The dependence on geometry must be called out. Features visible in the ocean spectra at different operating geometries will not necessarily appear in the SAR image. For example, this processing takes the same swath of SAR image and rederives the ocean spectra given three different incidence angles (the angle at which the radar beam contacts the ocean surface). Figure 12 shows the outputs of a geometry driven experiment. In each pane, the incidence angle was the only input altered. Notice how the SAR swaths are identical, but a feature in the ocean spectrum moves.

#### *An Iterative Approach*

Having seen that the conversion from ocean spectrum to SAR image spectrum heavily relies upon nonlinear and complicated MTFs, the challenge of creating an efficient inversion scheme becomes fully revealed. Hasselmann suggests that the correct path follows a normalized iterative approach with a weighting on a 'first

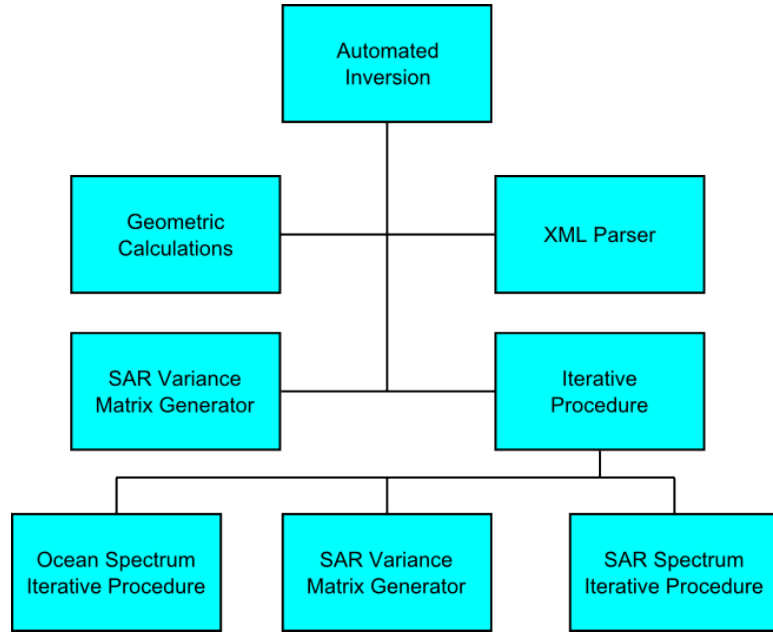


Figure 11. Visual Representation of How Components in the Inversion Process Interact

guess' ocean spectrum. For the purposes of this section, let  $F$  be the wave spectrum and  $P$  be the SAR image spectrum.

In order to iteratively solve for these ocean spectra, 'first guess' ocean spectra are generated to start the process. Let  $\hat{P}$ ,  $P$ ,  $\hat{F}$ , and  $F$  be the observed SAR, generated SAR, 'best guess' ocean, and the computed ocean spectra, respectively. The iterations aim to minimize the cost function

$$J = \int [P(k) - \hat{P}(k)]^2 dk + \mu \int \left[ \frac{[F(k) - \hat{F}(k)]}{[B + \hat{F}(k)]} \right]^2 dk \quad (4.1)$$

where  $\mu$  weights the function to reflect relative confidence in the guessed ocean spectrum. The variable  $B$  here compensates for when  $\hat{F}(x) = 0$ . For the purposes of Project Ocean Winds,  $B$  was set to the MATLAB data value  $\epsilon$ .

This  $J$  is then computed several times over with the differences of successive

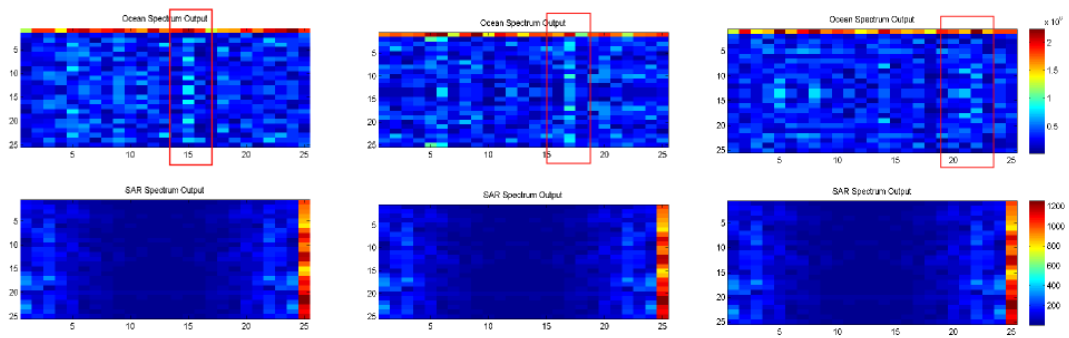


Figure 12. Ocean Spectra Processed from the same SAR Swath Using  $30^\circ$ ,  $37^\circ$ , and  $42^\circ$  Incidence Angles (respectively)

evaluations being compared to a tolerance parameter. For each iteration a new SAR spectrum is generated based upon the newly accepted ocean spectrum. Once the difference no longer surpasses the tolerance parameter, the computed ocean spectrum is accepted as the best estimate of the actual spectrum. Note that the  $\mu$  in this formula is not the same as the damping factor from the hydrodynamic MTF. The weighting factor  $\mu$  here follows the formula

$$\mu = 0.1\hat{P}_{max}^2, \quad (4.2)$$

as suggested by [Hasselmann and Hasselmann (1991)].

Because each iteration requires the processing of an ocean spectrum to a SAR image through the original conversion, the reversal process requires the computation of (3.10) many times. It becomes clear that this process makes hundreds of thousands of calls to MTFs in one computation, which takes extremely large amounts of computation time and power.

Recalling that the MTFs in use are nonlinear, the inversion is only quasi-linear.

Thus the process works albeit slowly and less accurately for small scale images. Regardless of the quasi-linearity and cumbersome nature of the computation, it should be noted that Hasselmann's original research was performed on data recovered at least six years old when the article was published and with less advanced computers. Thus, perhaps with a new technique, taking advantage of new high resolution data and better computers, the process will evolve to be more efficient.

### *A New Direction*

Although currently under development, the group at Project Ocean Winds believes that a pixel by pixel approach may be more suitable. The idea would be to have the algorithm process each pixel according to a neighborhood around it. Since the process is still under development, the stages of analysis on this style of inversion scheme has not come to fruition.

## CHAPTER 5

### AZIMUTHAL CUTOFF FACTOR

Recall that our discussion of azimuthal displacement led to a heavy reliance on geometry. To account for this, in order to validate the cutoff factor from azimuthal displacement, several steps must be taken first. Primarily, the metadata provided for each image must be parsed to provide the appropriate information, allowing for the entire analysis to occur for each individual SAR image. At this point, the implementation presented in this thesis illustrates the collection, showing exactly how the satellite traversed the scene. Next, several computations provide data to the formula, resulting in the cutoff factor.

#### *Theoretical Description of Azimuthal Cutoff*

The overarching concern from azimuthal displacement was the ability for scatterers to not only appear shifted but for the wave field to blur due to heterogeneous motion. By computing the cutoff factor, it is possible to design collections that will have certain portions of the spectrum visible. Considering the physics involved in the MTFs interacting together, the cutoff factor should resemble a longer, more complicated expression. However, the electromagnetics, hydrodynamics, and collection geometry inherent in the computations do not force the factor to be unreasonably difficult to understand. Hasselmann finds that the azimuthal cutoff factor causes the conversions discussed previously to be nonlinear. In fact the explicit statement of

the factor

$$\Xi = e^{-k_x^2 \xi'^2}, \quad (5.1)$$

where  $k_x$  is the wavenumber component in the direction of the  $x$  direction of the satellite image (dependent on making a right hand coordinate system with the azimuth) and  $\xi'$  is the mean square azimuthal displacement of scatterers. Fortunately, the computation of  $\xi'$  involves terms already in use at other points in processing, namely

$$\xi'^2 = \beta^2 \int |T_k^v|^2 F(k) dk. \quad (5.2)$$

To validate that the expression for cutoff, an empirical data source must provide ground truth to combine with the spectral values from processed images. Only in this manner, will the cutoff factor definitively be ruled as compatible or not with higher resolution data.

### ***Empirical Data Sources***

In order to verify experimental calculations are correct, ground truth data must be acquired. Since images are taken over open ocean scenes, the most reliable data is obtained through the network of buoys maintained by the National Oceanic and Atmospheric Administration (NOAA) [NOAA (NOAA)] and other such organizations. The original data takes consisted of single and dual polarization images taken of two locations. Later data was taken from alternate locations based upon buoy data available.

The Pacific Northwest and Gulf of Mexico provided interesting wind patterns to examine. Thus for the initial data, scenes were located off the coast of Tillamook, OR, USA and over Walker Ridge in the Gulf. With the incursion of the polar vortex in the winter of 2013-2014, the Gulf of Maine provided an excellent location

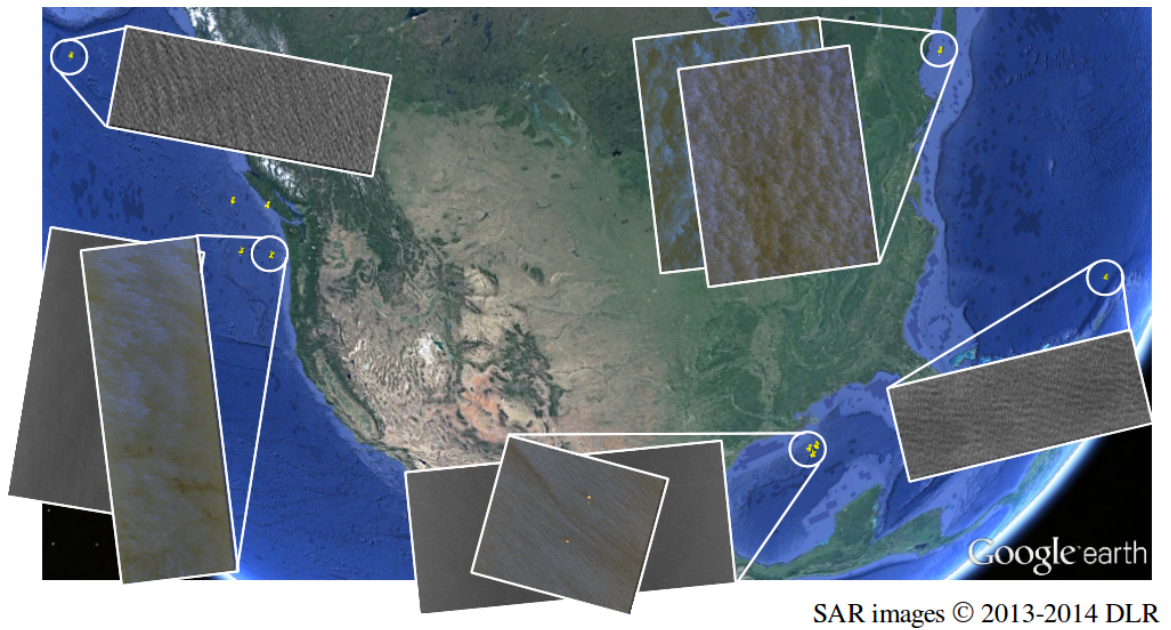


Figure 13. Scenes of Data Collections and Associated Images

to retrieve data from the Northeastern Regional Association of Coastal and Ocean Observing Systems (NERACOOS) buoys.

The constant rain fronts battering the Oregon coast suggested a pretty consistent wind flow inland. With varying speeds, the images from this area allow for the honing of wind speed estimation. NOAA buoy 46089 near Tillamook provided continuous wind speed measurements along with the values of spectral wave densities and principal wave direction.

In contrast, the Gulf of Mexico is known as a hotbed for major weather events. The hurricanes for which the Gulf is known exemplifies the chaotic wind patterns of the area. While hurricanes do not originate in the Gulf, often the paths they take change in the Gulf suggesting a wide variety of wind directions. The angular component of the analysis would need to be able to pick up these slight differences. Thus NOAA 42360 at Walker Ridge helped lock down ocean current, wind speed

Table 1. Summary of Ground Truth Buoys

Location	NOAA Number	Wind Speed	Wind Direction	Current Speed	Current Direction	Spectral Wave Density	Principal Wave Direction
Tillamook,OR	46089	X	X			X	X
Walker Ridge	42360	X	X	X	X		
Jordan Basin	44037	X	X	X	X		
Alaska	46066	X	X			X	X
Puerto Rico	41043	X	X			X	X
Martinique	41041	X	X			X	X

and direction data, but lacked wave data. The unforeseen difficulty came from 42360 being anchored to an oil platform, thus the images for the Gulf provided an excellent demonstration of man made structure and boat interference.

For the second data collection, a buoy located over the Jordan Basin in the Gulf of Maine, NERACOOS M01 (NOAA 44037), provided us the best possible data. Since these images were only received a few weeks before this thesis, the data has not been fully analyzed, but is indeed underway.

An additional collection was made for an experimental high resolution product. Scenes were chosen near Alaska, Puerto Rico, and Martinique.

As a note to the difficulties of ground truth, while NOAA and NERACOOS buoys have provided sufficient data, the exact location of the buoys differs slightly from the listing on NOAA's website. Thus while the buoy may not be present in scene, the location should be close enough to allow for rough analysis.

### *Validation*

The theoretical model for the displacement cutoff factor, previously validated against the Seasat and SIR-B data, may be compared to measurements taken off the SAR image spectrum directly. Beginning with computing the spectral gap and then combining this gap with geometry parameters and buoy measurements, the validity of Hasselmann's cutoff in terms of high resolution images may be assessed. The spectral gap, the distance between the origin and next spectral peak, is shown in Figure 8.

Given the spectral wave density, stated in the magnitude of height for waves at a frequency  $f$ , the expected value formula may be used to determine the mean squared height displacement

$$E[h^2] = \frac{1}{2\pi} \int \Phi(f) df. \quad (5.3)$$

The derivative of this function gives the orbital velocity of a particle on the surface of the ocean

$$E[v^2] = \int f \Phi(f) df. \quad (5.4)$$

Due to SAR collection geometry, there is a modulation due to wind speed so that

$$E[w^2] = E[v^2](\cos^2 \phi \sin^2 \theta + \cos^2 \theta), \quad (5.5)$$

where  $\phi$  denotes the angle between the wind and look directions and  $\theta$  is the incidence angle. The first term in the transfer function describes a modulation in the surface velocity, while the other corresponds to a modulation in the vertical component of velocity. Recalling that  $\rho$  is the slant range and  $U$  is the platform velocity, the azimuthal displacement is given by

$$E[\xi^2] = \frac{\rho^2}{U^2} E[w^2]. \quad (5.6)$$

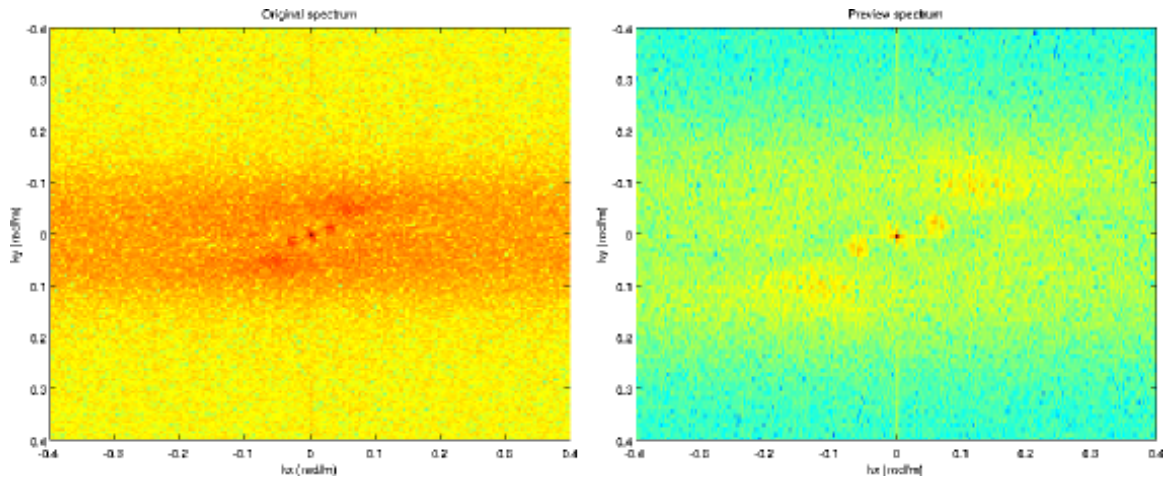


Figure 14. Spectra of an Original SAR with Visible Spectral Width (left) and Preview Image with Visible Spectral Peaks (right).

The half decayed cutoff may be computed by solving

$$\frac{1}{2} = e^{-k_x^2 \xi^2}. \quad (5.7)$$

This equation comes about as the azimuthal displacement is half the spectral width (as shown in Figure 8).

Unfortunately, the correct data was not available for the Gulf of Mexico images in order to compute the azimuthal displacement cutoff factor.

Hasselmann's theoretical expression performed extremely well on high resolution data [Table 2]. After these computations validated the theory behind the cutoff, other pieces in the research of Project Ocean Winds members began to fit into place. At the time of writing, new experimental data from a completely experimental mode demonstrated the importance of the azimuthal cutoff, since displacement was visible in the actual image.

Table 2. Summary of Azimuthal Cutoff Calculations

Parameter	Source	Portland single	Portland dual	Units
Spectral peak	Buoy	0.13	0.09	rad/m
Wind direction	Buoy	350°	262°	deg true N
Slant range	DLR	796	700	km
Satellite speed	DLR	7.7	7.7	km/s
Incidence angle	DLR	44°	42°	deg from vert
Look direction	DLR	260°	91°	deg true N
Az. displacement	Eq. (2.1)	15.5	14.3	m
Az. cutoff	Eq. (5.1)	0.053	0.058	rad/m
Az. cutoff	Image	0.055	0.05	rad/m
Percent error		-2.3%	16%	

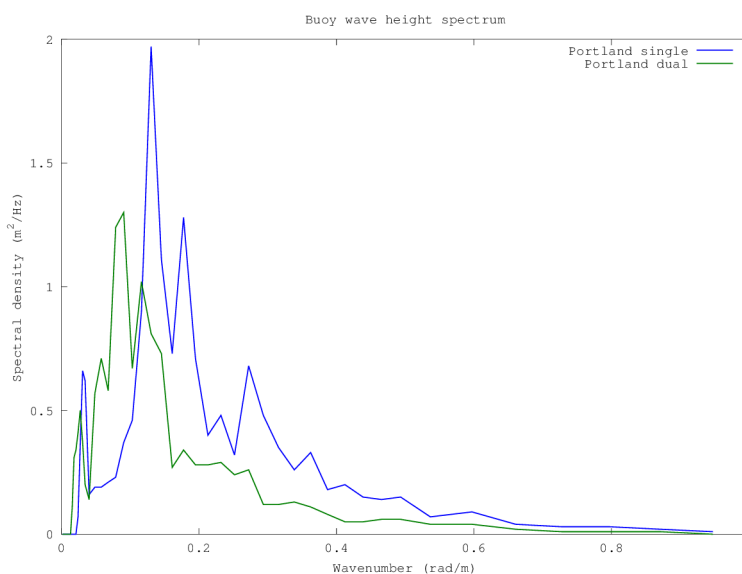


Figure 15. Buoy Spectra Used in Measurement for Azimuthal Cutoff Computation.

## CHAPTER 6

### CONCLUSIONS, CONTINUATION, AND FUTURE PLANS

Recall that in the introduction, limitations were explicitly stated. However, the mere fact that analysis of this level, conducted on high resolution satellite data, was performed by a small scale research team at a university with only internal funding speaks to the advancement in scientific contribution and feasibility of satellite research. The validation of Hasselmann's azimuthal cutoff factor allows for further advance in Project Ocean Winds and scientific research in general. This validation was also the first known attempt of its kind to reconcile lower resolution algorithms and higher resolution data processing. The relationship developed between lower resolution ocean spectra and SAR image spectra becomes viable for high resolution data, to a certain extent.

The research being done at American University on the measurement of wind turbulence over the ocean has farther to go. However, the key continuations for the material presented in this thesis comes in the form of the pixel by pixel inversion and further study of how azimuthal displacement and azimuthal cutoff play a role in the higher resolution imaging technology. The streamlining of the entire algorithm processing chain for Project Ocean Winds is another priority. With several members producing their own code, the group of researchers at Project Ocean Winds must sync their programs to seamlessly run together.

**APPENDIX A**  
**ABBREVIATIONS AND ACRONYMS**

DLR - German Aerospace Center

SIR - Shuttle Imaging Radar

OTF - Optical Transfer Function

MTF - Modulation Transfer Function

RAR - Real Aperture Radar

SAR - Synthetic Aperture Radar

NERACOOS - Northeastern Regional Association of Coastal and Ocean Observing Systems

NOAA - National Oceanic and Atmospheric Association

NASA - National Aeronautic and Space Administration

## REFERENCES

- CSA. “Radarsat-2.” Available at <http://www.asc-csa.gc.ca/eng/satellites/radarsat2/> (2014/04/20).
- Feindt, Folkart (1985). *Radar-Rckstreuexperimente am Wind-Wellen-Kanal bei sauberer und filmbedeckter Wasseroberflche im X-Band (9.8 GHz)*. Ph.D. thesis, University of Hamburg.
- Hasselmann, Klaus and Susanne Hasselmann (1991). “On the nonlinear mapping of an ocean wave spectrum into a synthetic aperture radar image spectrum and its inversion.” *Journal of Geophysical Research* 96(C6), 10713–10729.
- Keller, W.C. and J.W. Wright (1975, Feb). “Microwave scattering and the straining of wind-generated waves.” *Radio Science* 10(2), 139–147.
- Lange, P. and H. Hühnerfuss (1978, Jan). “Drift response of monomolekular slicks to wave and wind action.” *Journal of Physical Oceanography* 8, 142–150.
- NASA. “Seasat 1978.” Available at <http://southport.jpl.nasa.gov/scienceapps/seasat.html> (2014/04/20).
- NASA. “Sir-a 1982.” Available at <http://southport.jpl.nasa.gov/scienceapps/sira.html> (2014/04/20).
- NASA. “Sir-b 1985.” Available at <http://southport.jpl.nasa.gov/scienceapps/sirb.html> (2014/04/20).
- NOAA. “National data buoy center.” Available at <http://www.ndbc.noaa.gov/> (2014/04/20).
- Robinson, Michael (2013, Dec). “Measuring ocean winds from space using a radar satellite.” Technical report, American University, Washington, D.C.
- Werninghaus, R. (2009, Mar). *TerraSAR-X Ground Segment Basic Product Specification Document*. German Aerospace Center (DLR).
- Zink, M. (2010, Jul). *TanDEM-X Ground Segment TanDEM-X Science Service System Manual*. German Aerospace Center (DLR).